JOURNAL OF COMPUTATIONAL PHYSICS 116, 226–246 (1995)

# Numerical Study of Sound Emission by 2D Regular and Chaotic Vortex Configurations

OMAR M. KNIO

*Department of Mechanical Engineering, The Johns Hopkins University, Baltimore, Maryland 21218*

AND

LUC COLLOREC AND DANIEL JUVÉ

*Laboratoire de Mécanique des Fluides et d'Acoustique, URA CNRS 263, Ecole Centrale de Lyon, 69131 Ecully, France*

Received March 18, 1994

The far-field noise generated by a system of three Gaussian vortices lying over a flat boundary is numerically investigated using a two-dimensional vortex element method. The method is based on the discretization of the vorticity field into a finite number of smoothed vortex elements of spherical overlapping cores. The elements are convected in a Lagrangian reference along particle trajectories using the local velocity vector, given in terms of a desingularized Biot–Savart law. The initial structure of the vortex system is triangular; a one-dimensional family of initial configurations is constructed by keeping one side of the triangle fixed and vertical, and varying the abscissa of the centroid of the remaining vortex. The inviscid dynamics of this vortex configuration are first investigated using non-deformable vortices. Depending on the aspect ratio of the initial system, regular or chaotic motion occurs. Due to wall-related symmetries, the far-field sound always exhibits a time-independent quadrupolar directivity with maxima parallel and perpendicular to the wall. When regular motion prevails, the noise spectrum is dominated by discrete frequencies which correspond to the fundamental system frequency and its superharmonics. For chaotic motion, a broadband spectrum is obtained; computed soundlevels are substantially higher than in non-chaotic systems. A more sophisticated analysis is then performed which accounts for vortex core dynamics. Results show that the vortex cores are susceptible to inviscid instability which leads to violent vorticity reorganization within the core. This phenomenon has little effect on the large-scale features of the motion of the system or on low frequency sound emission. However, it leads to the generation of a high-frequency noise band in the acoustic pressure spectrum. The latter is observed in both regular and chaotic system simulations. 

## 1. INTRODUCTION

Point-vortex representations have long been used to simulate the motion of systems of concentrated vortices. The advantages of this approach are many, including its algorithmic simplicity and the efficiency of the representation. Simplified model solutions have proven to be useful in elucidating the underlying dynamics of a wide class of incompressible shear flows, namely those dominated by the essentially inviscid motion of 2D concentrated vortical structures.

Point-vortices have also been used to investigate the onset and properties of chaotic fluid motion [1]. In an unbounded domain, it has been established that a minimum of four point vortices are needed for chaotic motion to occur. This result derives immediately from the studies of Novikov [2] and Aref [3], which show that three-vortex systems in free space are characterized by regular trajectories. Subsequent studies [4, 5] indicated that this minimum can in fact be reached, as chaotic four-vortex problems were found and analyzed.

However, in the presence of a slip boundary, the presence of three point-vortices has been found sufficient for chaotic motion to occur. The study of Murty and Rao [6], which considered the evolution of point vortices inside a cylinder, provided an early example. These findings were later amplified in [7], which revealed that the presence of a potential boundary may play an important role in the transition to chaotic motion.

Due to its relevance to a large number of noise generation problems, the chaotic evolution of systems of concentrated vortices close to solid boundaries has motivated investigations of the sound emitted by such motion. Thus, Conlisk *et al.* [8] analyzed the evolution of chaotic and regular three-vortex systems above a flat boundary. Their results indicate that the chaotic behavior of the system results in a broadband near-field pressure spectrum. This problem was reconsidered by Collorec *et al.* [9] who performed a more detailed analysis of the noise radiation. In particular, their study shows that chaotic motion also results in a broadband far-field spectrum [10].

Unfortunately, the construction and implementation of



0021-9991/95 $6.00

point-vortex models inherently ignores the effects of core vorticity distributions and internal dynamics. Obviously, vortex core dynamics are expected to have little impact on the broad features of system evolution whenever concentrated vortices remain well-separated. However, the transition to chaotic motion is often accompanied by strong vortex interactions and by the development of violent strain fields. The occurrence of such phenomena raises some fundamental questions regarding both the evolution of the system and the corresponding noise emission. Thus, even in situations where vortices remain well-separated, the impact of core deformation on chaotic system behavior and radiated noise has not been fully investigated.

In this work, the issue is addressed using a two-dimensional vortex element method to simulate the evolution of the vorticity field. The present implementation also focuses on the same initial configurations previously considered in [8, 9]. This selection is motivated by the relative simplicity of the flow geometry which, nonetheless, allows us to observe a wide range of evolution regimes. Another advantage of the relatively simple configuration of the vorticity field is that it enables us to directly take advantage of acoustic analogy theory in order to calculate the far-field noise. Although Lighthill's original formulation [11] has proven to be useful in a large number of applications, the versions developed by Powell [12], Hardin [13], and Möhring [14] are preferred as they estimate the far-field pressure in terms of a convolution over the vorticity field [15]. However, since these formulations typically assume a compact three-dimensional vorticity field, their application remains complicated by our present restriction to two-dimensional flow [16]. In a first approach, this difficulty is avoided by restricting the convolution to a finite length along the axis of the vortices. The validity of this approximate approach is then tested using a detailed two-dimensional analysis recently proposed by Mitchell *et al.* [17].

In analyzing the impact of core dynamics on flowfield behavior, the adopted approach calls for comparing the predictions of three modelling approaches: (i) the point-vortex approximation, (ii) a frozen-core Gaussian model, and (iii) detailed vortex element computations. Construction of these models is summarized in Section 2, which also details procedures used to compute the acoustic farfield. Results of the simulations are given and discussed in Section 3. Major conclusions are summarized in Section 4.

## 2. FORMULATION AND NUMERICAL SCHEMES

### 2.1. Formulation

In all calculations presented, a two-dimensional, inviscid, incompressible, unsteady flow is assumed. Under these assumptions, the flowfield is governed by the vorticity transport and continuity equations which, in a right-handed coordinate system, $(x, y)$, are respectively expressed as

$$\frac{D\omega}{Dt} = 0 \tag{1}$$

$$\nabla \cdot \mathbf{u} = 0, \tag{2}$$

where $\mathbf{u}$ is the velocity vector, $t$ is time, $\omega \equiv \nabla \times \mathbf{u}$ is the vorticity, $D/Dt \equiv \partial/\partial t + \mathbf{u} \cdot \nabla$ is the material derivative, and $\nabla \equiv (\partial/\partial x, \partial/\partial y)$ is the gradient operator. The velocity field is related to the vorticity through the well-known Biot–Savart law [18],

$$\mathbf{u}(\mathbf{x}, t) = \int \omega(\mathbf{y}, t) \times \nabla G(\mathbf{x} - \mathbf{y})\, d\mathbf{y} + \nabla\phi, \tag{3}$$

where

$$G(\mathbf{x}) = \frac{1}{2\pi} \ln(|\mathbf{x}|) \tag{4}$$

is the Green's function of the 2D Poisson equation, and $\phi$ is a potential function needed to satisfy potential boundary conditions.

### 2.2. Flowfield Simulation

As previously mentioned, simulation of the governing equations is performed using a two-dimensional vortex method. Since these methods have been extensively discussed in the literature (*e.g.*, [19–20]), present implementations are briefly summarized. Construction of the numerical scheme starts with the discretization of the vorticity field into smoothed Lagrangian elements, using the expression [21–23]

$$\omega(\mathbf{x}, t) = \sum_{i=1}^{N} \omega_i(t) h_i^2 f_\delta(\mathbf{x} - \chi_i(t)), \tag{5}$$

where $\omega_i(t)$, $\chi_i(t)$, and $h_i^2$ respectively denote the vorticity, Lagrangian location, and "volume" of the ith vortex element, and $N$ is the total number of elements. In Eq. (5), $f_\delta$ denotes a rapidly decaying "spherical" core function used to smooth the particle vorticity; we let

$$f_\delta(\mathbf{x}) = \frac{1}{\delta^2} f\left(\frac{r}{\delta}\right), \tag{6}$$

so that $\delta$ represents the radius of the "sphere" where most of the vorticity of the element is concentrated. In this work, the second-order Gaussian core function

$$f(r) = \frac{1}{\pi} e^{-r^2} \tag{7}$$

is used. As shown by Beale and Majda [24], this choice yields an essentially second-order vortex element scheme.

According to the particle discretization given in Eq. (5),

the evolution of the vorticity and Lagrangian location of the elements must be obtained in order to determine the motion of the vorticity field. Since the locations $\chi_i(t)$ correspond to material particles, their evolution is governed by

$$\frac{d\chi_i(t)}{dt} = \mathbf{u}(\chi_i(t), t). \tag{8}$$

The velocity field is determined by inserting Eq. (5) into Eq. (3) and performing the integration; the result is expressed in terms of the desingularized Biot–Savart law,

$$\mathbf{u}(\mathbf{x}, t) = -\frac{1}{2\pi}\sum_{i=1}^{N}\Gamma_i\frac{(\mathbf{x}-\chi_i(t))\times\mathbf{k}}{|\mathbf{x}-\chi_i(t)|^2}\kappa_\delta(\mathbf{x}-\chi_i(t)), \tag{9}$$

where $\mathbf{k}$ is the unit normal to the plane of motion, $\Gamma_i \equiv \omega_i h^2$ is the circulation of the element, and $\kappa_\delta$ is the velocity smoothing kernel corresponding to $f_\delta$:

$$\kappa_\delta(\mathbf{x}) = \kappa\left(\frac{|\mathbf{x}|}{\delta}\right); \quad \kappa(r) = \int_0^r 2\pi\xi f(\xi)\, d\xi. \tag{10}$$

For $f$ given by Eq. (7), $\kappa(r) = 1 - \exp(-r^2)$. On the other hand, since we have restricted our attention to 2D inviscid incompressible flow, the Kelvin and Helmholtz theorems immediately imply that both the circulation and vorticity of the elements is constant. Thus, numerical integration of Eq. (8) is all that is required to complete the formulation of the method. In the calculations, a second-order predictor corrector scheme is used to advance the solution [25].

In some calculations, point-vortex schemes are used in lieu of the vortex method described above. The major difference between the two approaches is that in the point-vortex approximation a discrete desingularization of the velocity field is performed. Thus, for a collection of point-vortices specified as $\{\chi_i, \Gamma_i\}_{i=1}^N$, the discrete velocity field is given by

$$\mathbf{u}(\chi_j(t)) = -\frac{1}{2\pi}\sum_{i\neq j}\Gamma_i\frac{(\chi_j(t)-\chi_i(t))\times\mathbf{k}}{|\chi_j(t)-\chi_i(t)|^2}. \tag{11}$$

Implementation of the point-vortex scheme is similar to that of the vortex method: Eq. (11) replaces Eq. (9); the remaining aspects of the algorithms remain unchanged. (It is interesting to note that while Eq. (9) defines a smooth field quantity, Eq. (11) is only used to estimate the velocity of discrete vortices.)

### 2.3. Initial Conditions

In most calculations, we consider initial configurations corresponding to three equal-strength concentrated vortices located close to a solid potential boundary. The physical boundary coincides with the $x$-axis and restricts the motion of the vortices to the semi-infinite upper-half plane. Physical variables are normalized so that the circulation of the vortices $\Gamma = 2$. Meanwhile, the geometry of the initial configuration is normalized such that the triangle formed by the three vortices has one side fixed on the $y$-axis, $0.5 < y < 1$. The normalized coordinates of the remaining vortex are chosen such that its "height" $y = 0.75$, but its abscissa is taken as a variable parameter, $a \geq 0$ (Fig. 1). Except in point-vortex simulations, the vorticity distribution associated with the vortices is assumed to be Gaussian with standard deviation $\sigma$:

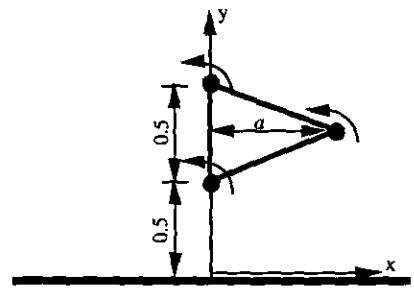


**FIG. 1.** Schematic illustration of the initial vorticity configuration.

$$\omega(r) = \frac{\Gamma}{\pi\sigma^2}\exp\left(-\frac{r^2}{\sigma^2}\right). \tag{12}$$

The selection of the initial vorticity configuration is motivated on one hand by its simplicity and on the other by previous theoretical and numerical considerations which lead us to expect a wide range of dynamical behavior [5, 8]. In particular, selection of the number of vortices reflects theoretical results which indicate that a minimum of three point-vortices moving close to a slip plane is needed for chaotic motion to be possible. Investigation of this aspect of the problem is presented Section 3.

We finally note that consideration of the potential boundary along the $x$-axis necessitates slight modification to the numerical scheme. The no-normal flow boundary conditions at the wall surface are enforced simply by accounting for the appropriate image of the vortex system.

### 2.4. Acoustic Far-field

The acoustic far-field is estimated, based on the computed evolution of the vorticity field. In doing so, two modelling approaches are applied. The first model relies on the Powell–Hardin formulation [12, 13], the second is an adaptation of the two-dimensional Green's function approach recently given in [17]. Since the details of the implementation differ significantly from one model to the other, these are summarized independently below.

*The Powell–Hardin Formulation*

The Powell–Hardin formulations is based on two major assumptions: (i) a 3D compact vorticity field and (ii) a compact

source region; *i.e.*, the size of the source region is small compared to the acoustic wavelength. (For the presently considered flow configuration, source compactness is reflected by the fact that the characteristic size of the vortex system, including the image vortices, is much smaller than the relevant acoustic wavelengths). The predicted acoustic far-field is given in terms of a convolution over the compact source region, as expressed by

$$p(\mathbf{x}, t) = \frac{\rho_o}{4\pi c_o^2} \frac{1}{|\mathbf{x}|} \frac{d^2}{dt^2} [\mathbf{d} \cdot \mathbf{y})(\mathbf{d} \cdot \mathbf{L})\, d\mathbf{y}]^*, \tag{13}$$

where $\mathbf{x} = (x_1, x_2, x_3)$ is the position of the listener, $c_o$ is the speed of sound, $\mathbf{L} \equiv -\mathbf{u} \times \omega$ is the Lamb vector, $\mathbf{d} \equiv \mathbf{x}/|\mathbf{x}|$, and the asterisk indicates evaluation at the delayed time,

$$t^* = t - |\mathbf{x}|/c_o. \tag{14}$$

In order to take advantage of the above formulation, we simplify the analysis by: (1) assuming a three-dimensional sound emission, (2) limiting the position of the listener to the $x$–$y$ plane, and (3) defining a finite "active emission zone" by restricting the contribution of the vorticity field to a distance $l$ along the spanwise direction. Implementation of these simplifying assumptions allows direct application of Eq. (13) to both point-vortex and vortex element computations. Derivation of the corresponding acoustic pressure predictions are briefly highlighted in the following.

In point-vortex calculations, the vorticity field is modelled as a collection of delta functions concentrated at the vortex locations. By (i) inserting the corresponding distribution into Eq. (13), (ii) using the velocity predictions given by Eq. (11), (iii) accounting for the image system of the vortices, and (iv) invoking the source compactness assumption, we get

$$p(\mathbf{x}, t) = -\frac{\rho_o}{4\pi} \frac{x_i x_j}{c_o^2 r^3} \frac{d^2}{dt^2} \left[ \iint y_i L_j \, d\mathbf{y} \right]^* \tag{15}$$

which yields

$$p(\mathbf{x}, t) = \frac{\rho_o}{2c_o^2 r} \frac{d^2}{dt^2} \sum_i \alpha_i, \tag{16}$$

where the summation is taken over the vortices in the top half plane,

$$\alpha_i = 2 \frac{\Gamma_i}{2\pi} \frac{x^2 \xi_i v_i - y^2 \eta_i u_i}{x^2 + y^2}, \tag{17}$$

$(\xi_i, \eta_i)$ are the components of the Lagrangian vector $\chi_i$, and, for brevity, the delayed time symbol has been omitted. Next, using the fact that the impulse of the system,

$$I = \sum_i \Gamma_i (\xi_i v_i - \eta_i u_i), \tag{18}$$

is a conserved quantity, Eq. (16) is simplified as

$$p(\mathbf{x}, t) = \frac{\rho_o}{\pi c_o^2 r} \frac{x^2 - y^2}{x^2 + y^2} \frac{d^2}{dt^2} \sum_i \Gamma_i x_i v_i. \tag{19}$$

A quadrupolar noise emission is predicted whose intensity and time evolution are determined by the "curvature of the moment of vorticity signal" as expressed by the summation term. However, the radiated noise directivity is not "rotating in time" as is the case in most applications. This result can be interpreted by noting that while the vortex system (which lies on the top half-plane) leads to rotating quadrupole emission, its image system generates a similar quadrupolar emission which rotates in the opposite direction. The combination of the "two emissions" is a single quadrupole with fixed directivity and maxima parallel and perpendicular to the wall. The vanishing emission at 45° and 135° inclination can be explained by noting that, for these inclination angles, the invariant expressed by Eq. (18) is recovered in Eq. (17), so that time derivatives cancel identically.

For vortex element calculations, derivation of the far-field pressure starts by substituting the vorticity and velocity expressions, Eqs. (5) and (9), respectively, into Eq. (13). Under the same assumptions previously invoked, the component form of the resulting expression is expressed as

$$p(\mathbf{x}, t) = \frac{\rho_o}{4\pi c_o^2 r^3} \frac{d^2}{dt^2} [-x^2 U + y^2 V + xyW], \tag{20}$$

where

$$U = \int x' v\omega \, dx' \, dy' \tag{21}$$

$$V = \int y' u\omega \, dx' \, dy' \tag{22}$$

$$W = \int (x' u\omega - y' v\omega) \, dx' \, dy', \tag{23}$$

where the integrals are taken over the entire $x$–$y$ plane. Due to symmetry about the $x$-axis and the fact that estimates are based on the same time delay, $W$ vanishes identically. It also turns out that $U = V$.

Thus, the problem is reduced to evaluation of a single integral. Unfortunately, if directly performed, this operation requires an excessive amount of computational overhead. To reduce this overhead, we first expand the integral in Eq. (21) by inserting the component form of Eqs. (5) and (9). After some lengthy but straightforward manipulations, Eq. (21) is recast as

$$U = -\frac{1}{2\pi} \sum_{i=1}^{N'} \Gamma_i \sum_{j=1}^{N'} \Gamma_j \left[ \iint \{x^2 + (x_i - 2x_j)x + x_j(x_i - x_j)\} \frac{\kappa_\delta(\mathbf{x} - \{\chi_i - \chi_j\})}{(\mathbf{x} - \{\chi_i - \chi_j\})^2} f_\delta(\mathbf{x}) \, d\mathbf{x} \right], \tag{24}$$

where $x = (x, y)$ is the variable of integration, $(x_i, y_i)$ are the components of the Lagrangian variable $\chi_i$, and $N'$ is introduced to indicate summation over the image system. Next, we resort to the polar decomposition of the vectors $\chi_i - \chi_j \rightarrow (R_{ij}\cos\phi, R_{ij}\sin\phi)$, and we implement the change of variables $\mathbf{x} \rightarrow (r\cos(\theta+\phi), r\sin(\theta+\phi))$, to obtain

$$U = -\frac{1}{2\pi}\sum_{i=1}^{N'}\Gamma_i\sum_{i=1}^{N'}\Gamma_j\,[-C_\delta(R_{ij}) - \cos(2\phi)D_\delta(R_{ij}) + (x_i - 2x_j)\cos(\phi)F_\delta(R_{ij}) + x_j(x_i - x_j)H_\delta(R_{ij})], \tag{25}$$

where

$$C_\delta(x) \equiv C\left(\frac{x}{\delta}\right);\quad D_\delta(x) \equiv D\left(\frac{x}{\delta}\right);\quad F_\delta(x) \equiv \delta F\left(\frac{x}{\delta}\right);\quad H_\delta(x) \equiv \delta^2 F\left(\frac{x}{\delta}\right) \tag{26}$$

$$C(x) \equiv \frac{1}{2\pi}\int_0^\infty \exp(-r^2)r^3 \int_0^{2\pi}\frac{1-\exp(-[r^2+x^2-2xr\cos\theta])}{r^2+x^2-2xr\cos\theta}\,d\theta\,dr \tag{27}$$

$$D(x) \equiv \frac{1}{2\pi}\int_0^\infty \exp(-r^2)r^3 \int_0^{2\pi}\frac{1-\exp(-[r^2+x^2-2xr\cos\theta])}{r^2+x^2-2xr\cos\theta}\cos(2\theta)\,d\theta\,dr \tag{28}$$

$$F(x) \equiv \frac{1}{\pi}\int_0^\infty \exp(-r^2)r^2 \int_0^{2\pi}\frac{1-\exp(-[r^2+x^2-2xr\cos\theta])}{r^2+x^2-2xr\cos\theta}\cos\theta\,d\theta\,dr \tag{29}$$

$$H(x) \equiv \frac{1}{\pi}\int_0^\infty \exp(-r^2)r \int_0^{2\pi}\frac{1-\exp(-[r^2+x^2-2xr\cos\theta])}{r^2+x^2-2xr\cos\theta}\,d\theta\,dr. \tag{30}$$

In a preprocessing step, the functions $C - H$ are tabulated on a fine grid; the corresponding vectors are linearly interpolated during the computations. Since the arguments of the functions are essentially differences which are computed during velocity evaluations, the acoustic pressure field is estimated at essentially no additional cost.

*Green's Function Approach*

As an alternative to the above formulation, the two-dimensional Green's function approach proposed in [17] is also adapted to the present problem. This approach aims at overcoming difficulties associated with directly applying 3D formulations—these were circumvented in the previous approach by assuming a compact "active emission zone." To do so, a 2D solution is derived based on combining Kambe's analysis [26] with a 2D Taylor's expansion of the velocity potential [27]. Matching near-field and far-field solutions, the acoustic pressure spectrum is expressed as

$$\hat{P}(\mathbf{x}, \bar{\omega}) = \frac{\rho\bar{\omega}^3}{8c_o^2}\frac{x_i x_j}{r^2}\hat{Q}_{ij}(\bar{\omega})H_2^1\left(\frac{\bar{\omega}r}{c_o}\right), \tag{31}$$

where $\bar{\omega}$ is the frequency, $H_2^1$ is a Hankel function, and $\hat{Q}_{ij}$ is the Fourier transform of the second moments of vorticity,

$$Q_{ij}(t) = \int y_i(\mathbf{y}\times\omega(\mathbf{y},t))_j\,d\mathbf{y}. \tag{32}$$

Thus, to adapt this approach to the present calculations, all that is needed is the time evolution of $Q_{ij}$. For brevity, the procedure is only described for point-vortex calculations. Accounting for the image system of the vorticity, the second-order moments are obtained by a straightforward calculation; we have

$$[Q_{ij}] = \begin{bmatrix} \sum_{i=1}^{N'}\Gamma_i\xi_i\eta_i & 0 \\ 0 & -\sum_{i=1}^{N'}\Gamma_i\xi_i\eta_i \end{bmatrix}, \tag{33}$$

where $(\xi_i, \eta_i)$ denote the components of the Lagrangian positions of the point-vortices. Once these second moments are computed, the pressure spectrum is obtained by inserting the transform of the signal results into Eq. (31). It is interesting to note that the structure of the matrix given in Eq. (33) implies the same sound directivity predicted by the Powell–Hardin formulation.

## 3. RESULTS AND DISCUSSION

The dynamics of the vortex systems described in Section 2.3 are investigated using two modelling approaches. In the first approach, core dynamics are neglected. The behavior of the simplified system and the noise emission are studied using both the point-vortex approximation and smoothed Gaussian vortices. Corresponding results are discussed in Section 3.1. The effects of core deformation are then examined using the vortex element method discussed in Section 2.2. Here, the vortex cores are discretized using a large number of vortex elements, whose motion is used to compute the dynamics of the system as well as sound emission. Results of these simulations are given in Section 3.2.

### 3.1. Non-deformable Core Model

As previously mentioned, this simplified analysis is conducted using both point-vortex and smoothed Gaussian vortices. In the former calculations, the initial conditions are specified

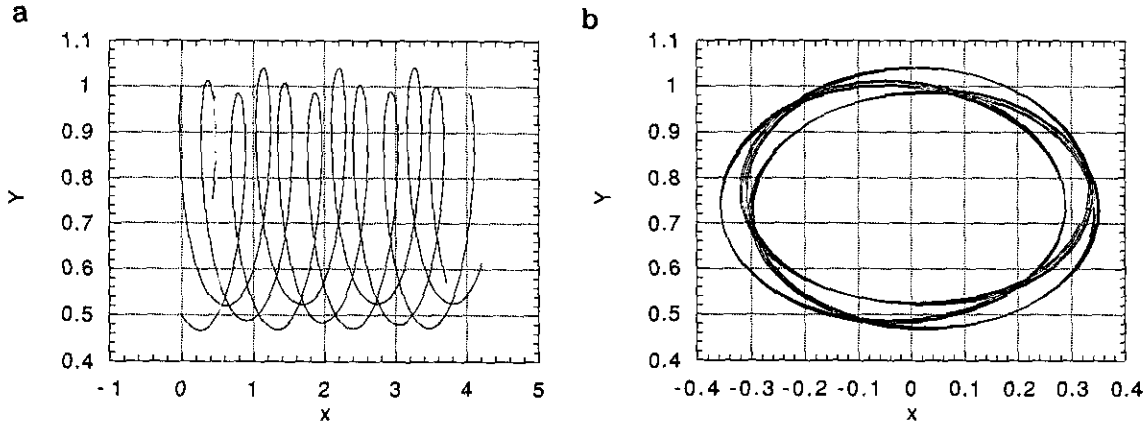


FIG. 2. Trajectories (a) and centered coordinates (b) of the point vortices for a system configuration with $a = 0.433$.

in terms of the initial strengths and locations of the vortices. The calculations are thus used to examine the effect of the initial configuration parameter $a$ on the behavior of the system. In smoothed vortex calculations, a "frozen" Gaussian core distribution is assumed. The core radii are measured in terms of the standard deviation $\sigma$ of the Gaussian. In order to compare between point-vortex and smoothed vortex predictions, a small value $\sigma = 0.05$ is selected (see Section 3.2).

*Dynamics*

The dynamics of the vortex system are interpreted in terms of the computed trajectories of individual vortices. Selected results are shown in Figs. 2–4 respectively for initial configuration parameters $a = 0.433$ (equilateral triangle), $a = 0.11$ (isosceles triangle which represents an intermediate "transitional" case), and $a = 0$ (degenerate case in which the three vortices are aligned). The deformation of the system is also illustrated by defining "centered" coordinates, measured in a reference frame attached to the centroid of the system,

$$\chi_c = \sum_{i=1}^{3} \Gamma_i \chi_i \Big/ \sum_{i=1}^{3} \Gamma_i. \tag{34}$$

Using the symmetries of the system, it is easily observed that the motion of the centroid is parallel to the wall. Thus, by absorbing translative motion, centered coordinates enable us to focus on the deformation of the system. In addition, we may regard these coordinates as a projection of the dynamical system and the corresponding trajectories as a phase portrait.

For an initial configuration with $a = 0.433$, Fig. 2 shows that, as the system propagates downstream, the point-vortices undergo a circular motion around the centroid. The motion of the centroid itself is nearly uniform, showing less than 1% variation in the propagation velocity. The trajectories are predominantly regular and are observed to be nearly identical from one rotation cycle to the other. (The computations predict a normalized rotation cycle frequency $f_r \approx 0.6$). Meanwhile, examination of the centered coordinates reveals that a weak deformation of the system occurs, as the corre-

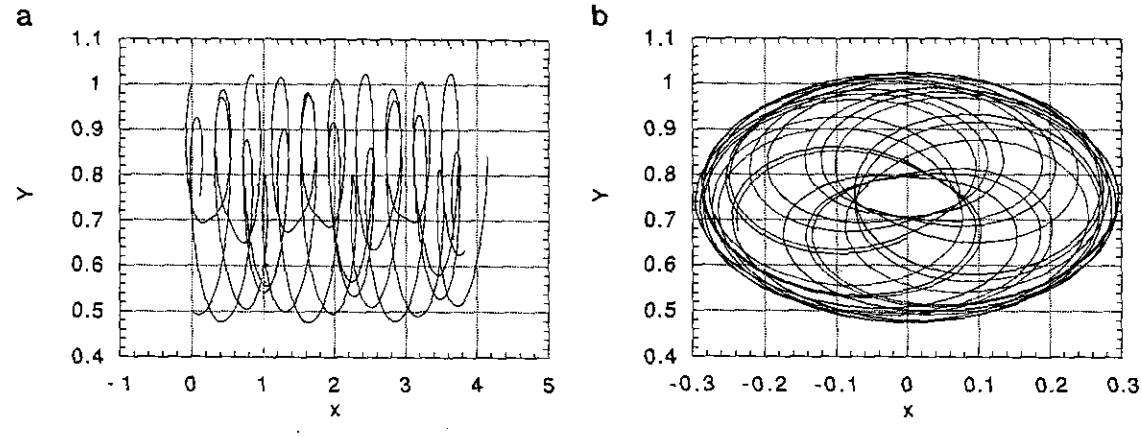


FIG. 3. Trajectories (a) and centered coordinates (b) of the point vortices for a system configuration with $a = 0.112$.

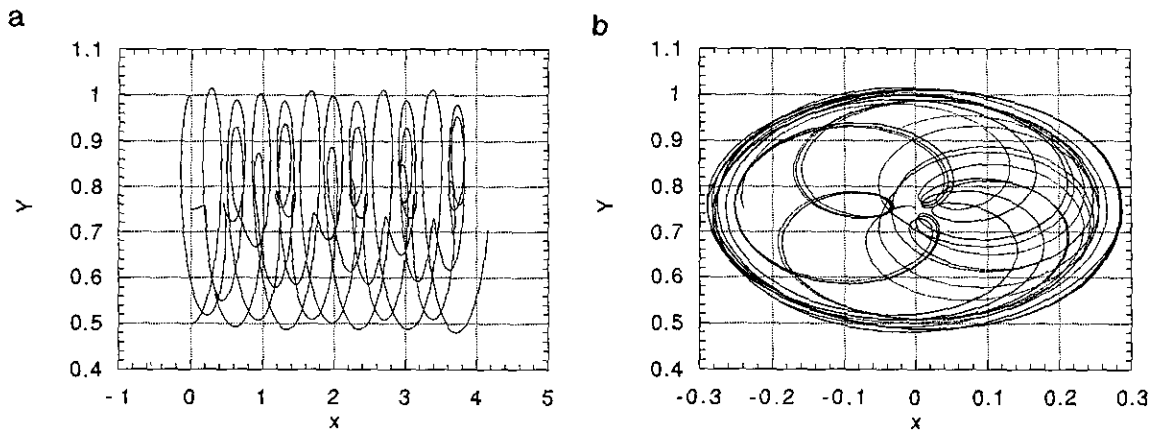


**FIG. 4.** Trajectories (a) and centered coordinates (b) of the point vortices for a system configuration with $a = 0$.

sponding trajectories are confined to a thin disk around the system centroid. In fact, the shape of the centered trajectories suggests that quasi-periodic motion occurs. This expectation is confirmed by a Fourier transform of the corresponding signals (not shown) which shows that the spinning of the system can be described by a discrete set of frequencies. The lowest frequency—the fundamental mode—corresponds to one rotation cycle around the centroid; the remaining frequencies appear as higher order harmonics of the fundamental.

When the initial configuration parameter is decreased to $a = 0.11$, considerable differences in the dynamics of the system are observed. The vortices no longer rotate regularly around their centroid; occasionally, high-curvature spinning motions occur, as indicated by the appearance of small knots in the computed trajectories (Fig. 3). It is also interesting to note that the centered coordinate curves now describe a wide annulus. In particular, the quasi-periodic behavior observed in the previous case is not recovered.

The departure from regular quasi-periodic motion is even more dramatic in the case $a = 0$. As shown in Fig. 4, the trajectories of the point vortices are highly convoluted, and the appearance of small knots is frequent. Meanwhile, examination of the motion in the centered coordinate system shows that the trajectories almost fill an entire circle around the centroid of the system. This suggests that a transition to chaotic behavior has occurred. In order to further examine the situation, the Lyapunov exponents associated with each Lagrangian coordinate are computed. Since larger exponents are indicative of more chaotic system behavior, we focus our attention exclusively on the leading exponent, $\lambda$. The procedure for obtaining the corresponding estimates are similar to those described in [28]. It is based on locally perturbing the location of the vortices, one at a time, and computing the divergence of the trajectories, measured in terms of the Euclidean distance between perturbed and unperturbed Lagrangian locations. The results of this exercise are summarized in Fig. 5, which depicts the dependence of $\lambda$ on $a$ for both point-vortex and Gaussian model calculations. In accordance with our previous expectation, a transition to chaotic motion is observed to occur around $a = 0.11$. As $a$ decreases below this value, the leading Lyapunov exponents increase abruptly from very small values to a plateau of height 1.5.

Finally, we note that essentially the same behavior is observed in the non-deformable Gaussian model. This is not surprising since the non-deformable Gaussian calculations yielded almost identical trajectories (not shown). Consequently, it is emphasized that the observed dynamics reflect the properties of the modelled system and are not affected by the modelling approach.

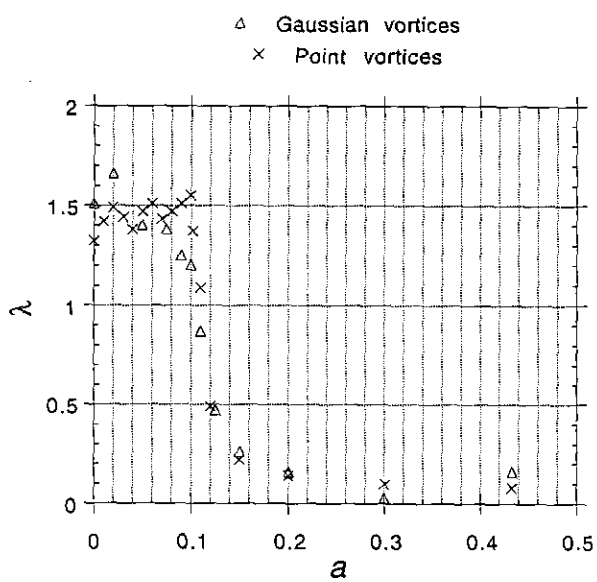


**FIG. 5.** Lyapunov exponents vs. configuration parameter $a$ based on point vortex calculations (×) and non-deformable Gaussian model with $\sigma = 0.05$ (Δ).

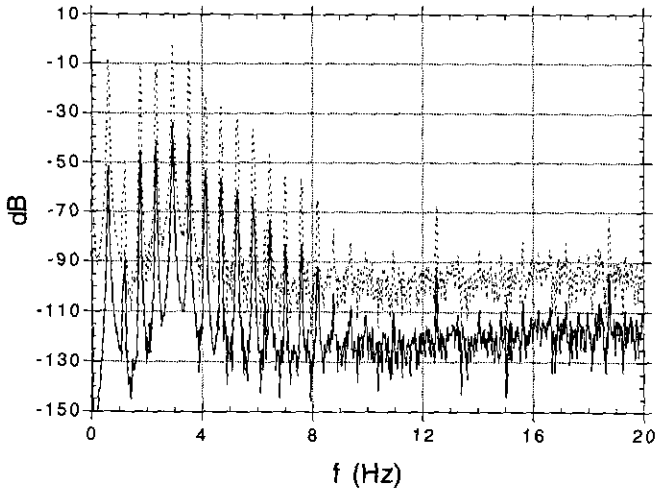


**FIG. 6.** Acoustic pressure spectra for an initial system configuration with $a = 0.433$, estimated using Eq. (19) (solid) and Eq. (31) with $\omega_{min} r/c_0 = 10$ (dashed).

*Sound Emission*

There appears to be a strong relationship between system behavior and radiated noise. To highlight this relationship, the far-field acoustic pressure spectra are computed using both the predictions of the Powell–Hardin formulation and the 2D Green's function approach. Since we are primarily interested in the structure of the acoustic spectrum, constant terms and (the quadrupolar) spatial dependence are factored out from the pressure predictions. The remaining time signal is then transformed to Fourier space and interpreted as a frequency spectrum. Results for initial configurations with $a = 0.433$ and $a = 0$ are shown in Figs. 6 and 7, respectively. Below, we attempt to relate the structure of these spectra and the predicted noise levels to the dynamics of the system.

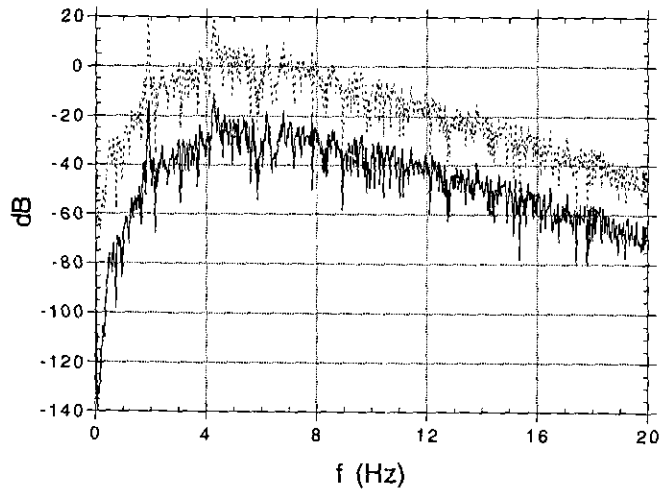


**FIG. 7.** Acoustic pressure spectra for an initial system configuration with $a = 0$, estimated using Eq. (19) (solid) and Eq. (31) with $\omega_{min} r/c_0 = 10$ (dashed).

The quasi-periodic motion obtained for an initial configuration with $a = 0.433$ appears to be reflected in the far-field pressure spectrum. In this case, Fig. 6 shows that the spectrum is dominated by a discrete set of harmonics. Detailed comparison of these acoustic frequencies with those characterizing vortex motion reveals that the first peak in the pressure spectrum corresponds to the "fundamental spinning frequency" of the system. This result is not surprising, in light of the large and well-established predictions in simpler configurations having similar dynamics—in particular, those of a pair of corotating point-vortices [17]. Meanwhile, the remaining frequencies appear as superharmonics of the fundamental. The first few harmonics have amplitudes of the same order as the fundamental, but the spectrum decays rapidly as we move to higher frequencies.

On the other hand, the sound emission calculated for the "chaotic" solution corresponding to an initial configuration having $a = 0$ has radically different features from the previous one. As shown in Fig. 7, the far-field noise is characterized by a broadband spectrum. The bandwidth of the noise emission, estimated by comparing the high-frequency decay of the spectra, is as about twice as large as in the previous case ($a = 0.433$, Fig. 6). In addition, while the peak sound intensities are assumed at about the same frequency, the corresponding soundlevels are roughly 30 dB higher than those computed before. Thus, the transition to chaotic motion is accompanied by a substantial increase in noise emission and a transition from a decaying discrete spectrum to a broadband spectrum with a slower frequency decay rate.

We conclude this section with a comparison of the acoustic pressure predictions corresponding to the selected formulations; in particular, justification for our adaptation of the 3D Powell–Hardin formulation is provided. It is first noted that, while the computed noise levels are not identical, the structure of the spectra predicted using both formulations is essentially the same. Regarding the origin of the amplitude difference, we first note that the decay laws of both formulations are not the same. In the Powell–Hardin formulation, the acoustic pressure amplitude decays as the inverse power of the distance from the acoustic source, as should be expected in a 3D formulation. This may be immediately verified by inspecting the form of Eq. (15). Meanwhile, for the 2D Green's function approach, an acoustic pressure decay scaling with the square root of the distance from the source is anticipated. To verify this behavior, which is implicitly embedded in the 2D expressions, we resort to the integral representation of the Hankel function [29] to recast Eq. (31) as

$$P(\mathbf{x}, t) = \beta_{ij} \sqrt{2c_o/\pi r} \int_0^\infty \exp(-\xi)\xi^{3/2} \int_{-\infty}^{+\infty} \left(\omega - i\frac{\xi c_o}{r}\right)^{3/2} \omega \hat{Q}_{ij}(\omega) \exp\left[-i\omega\left(t - \frac{r}{c_o}\right)\right] d\omega\, d\xi, \tag{35}$$

where

$$\beta_{ij} \equiv \frac{\rho x_i x_j}{8c_o^2 r^2} \frac{\exp(-i(5\pi/4))}{\Gamma(5/2)}. \tag{36}$$

The anticipated pressure dependence on listener location is now evident in Eq. (35). In addition, the form of this expression can be used to explain the observed similarity in pressure spectra. To do so, we note that the higher contributions are due to locations close to the observation plane, i.e., small $\xi$ values. These qualitative predictions may also be appreciated by inspecting the simplified form of Eqs. (35)–(36),

$$P(\mathbf{x}, t) \approx -\frac{\rho x_i x_j}{8c_o^2 r^2} \exp\left(-i\frac{5\pi}{4}\right) \sqrt{2c_o/\pi r} \int_{-\infty}^{+\infty} \omega^{5/2} \hat{Q}_{ij}(\omega) \exp\left[-i\omega\left(t - \frac{r}{c_o}\right)\right] d\omega, \tag{37}$$

which is derived by using the large-argument asymptotic form of the Hankel function instead of the above integral representation.

Unfortunately, the complexity of the 2D expressions does not allow us to isolate the spatial and temporal terms in the acoustic pressure predictions. In particular, a one-to-one comparison between the two formulations was not possible. When using the 2D Green's function formulation, selection of different values of $r$ was found to affect the amplitude but not the structure of the predicted noise spectrum. (In particular, the value of $r$ used to generate the "2D curves" of Figs. 6 and 7 was selected so that the far-field assumptions is satisfied; we used $\omega_{\min} r/c_o = 10$, where $\omega_{\min}$ is the angular frequency of the first peak in the sound spectrum. The latter is also used to verify that the compactness assumption holds; using a normalized cutoff frequency $f_{\max} = 20$, the ratio of the source region size to the shortest wavelength is approximately 1:10). Since we are primarily interested in the radiated noise spectrum and since both formulations are found to yield nearly identical spectra, the Powell–Hardin formulation is selected in the following computations. This choice was based purely on the simplicity of the adapted 3D expressions, which enable simple isolation of the time-dependent behavior of the acoustic pressure.

### 3.2. Deformable Core Model

In this section, a more realistic physical model is adopted which accounts for the vortex core deformation. To capture the core dynamics, the model emphasizes numerical discretization of the core vorticity distribution using a large number of vortex elements. The primary objective of this extension is to analyze the impact of the dynamics ignored by the previous models on the characteristics of noise emission.

While performing the computations, however, issues concerning the numerical discretization arose which had to be carefeully addressed. The first concerns the effect of numerical discretization on the behavior of the solution. In particular, when chaotic motion occurred, a fine discretization was found necessary to ensure that the computed integral quantities are independent from the selected values of the numerical parameters. In addition, we had to verify that the large-scale features of the solutions computed using deformable and non-deformable models are in fact similar, so that comparison of the results can be performed. Surprisingly, this turns out to be the case.

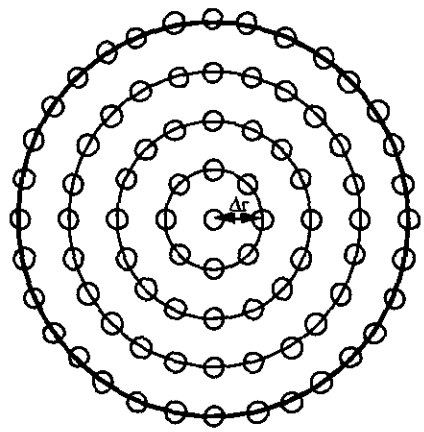


**FIG. 8.** *Schematic illustration of the computational grid used to initialize vortex element calculations.*

Due to the importance of the numerical discretization, we start with a somewhat detailed account of the numerical discretization. Next, the computational study of the impact of numerical parameters is briefly summarized. Results concerning far-field noise spectra are then discussed.

*Discretization*

The procedure for vortex core discretization is essentially an adaptation of that discussed in [25]. To summarize, vortex elements are initially distributed on a computational grid which is constructed by first defining $N_r$ radial stations within the core, which describe circles that are concentric with the location of the Gaussian core. The first radial station is simply identified with the center of the vortex core and is represented by using a single element. The remaining radial stations are separated by a distance $\Delta r$ in the radial direction, each carrying $8(i-1)$, $i = 2, \ldots, N_r$, vortex elements distributed uniformly around the circumference. Thus, the second radial station has eight elements, the third 16, and so on (Fig. 8).

Once the initial grid is selected, the vortex strengths are initialized using a collocation procedure which requires that the discretized vorticity distribution matches the initial condition at the centers of the elements. Accordingly, a linear system of equations is formed by setting the right-hand side of Eq. (5) equal to the intended values, obtained by evaluating Eq. (12)

**TABLE I**

Summary of Discretization Parameters

| Grid | $N_r$ | $N$ | $N_t$ | $\Delta r/\sigma$ | $\delta/\sigma$ |
|---|---|---|---|---|---|
| 1 | 4 | 49 | 147 | 0.43 | 0.84 |
| 2 | 5 | 81 | 243 | 0.325 | 0.83 |
| 3 | 6 | 121 | 363 | 0.26 | 0.82 |
| 4 | 7 | 169 | 507 | 0.231 | 0.82 |

at the $\chi_i$'s. Inversion of this sytem then yields the strengths of the elements. During this procedure, iteration over the core values is performed in order to ensure overlap among neighboring elements and to minimize the error between discretized and assumed vorticity distributions [25].

In the simulations presented below, four different computational grids are used. The latter are constructed by selecting grids having $N_r = 4$, 5, 6, and 7; the corresponding number of vortex elements $N = 49$, 81, 121, and 169, respectively. Since three vortices are present, the total number of vortex elements in the domain $N_t = 3N = 147$, 243, 363, and 507. Thus, the total number of elements is increased from one grid to the other, in order to examine the effect of the numerical resolution on the computed motion of the system. A summary of discretization parameters is provided in Table I. Recall that $\sigma$ denotes the standard deviation of the initial Gaussian vorticity distribution, while $\delta$ refers to the core size of individual vortex elements.

*Summary of the Numerical Study*

The adopted approach in the numerical study of computed solutions consists of first ensuring a time-accurate integration. To this end, a variable-step second-order predictor–corrector method is adopted, and stringent criteria for time-step refinement are incorporated. Accordingly, very small time steps are selected in the computations; the simulation of a few vortex turnover times is typically performed in over 100,000 iterations. Thus, the independence of the computed solution from the time-integration scheme and parameters is established for all reported calculations.

Consequently, we concentrate on studying the impact of spatial discretization on the behavior of the system. To limit the effort, we restrict our attention to the vortex system having initial configuration parameter $a = 0$. This choice is based on the results of the above computations, which indicate that the corresponding (point-vortex/non-deformable Gaussian) configuration exhibit chaotic dynamics having the highest estimated Lyapunov exponent. In other words, within the parameter range of interest, the selection is believed to provide the most challenging test for the computations. In addition, since we are interested in comparing our results with those of point-vortex computations, a small value of the core radius, $\sigma = 0.05$ is chosen.

Figures 9–11 show results of the computations, initialized respectively using grids having $N_r = 81$, 121, and 169; for brevity, the results for $N_r = 49$ are omitted. The computations are carried out until $t = 6$ (the rotation cycle of a single vortex $t \sim 1$). In all cases, the number of integration steps exceeded 220,000. Comparison of Figs. 9–11 shows that, while a close agreement in the large-scale structure of the flow is evident at small time ($t < 2$), significant differences among the predictions of various discretizations can be observed at later stages. This result is not totally unexpected, but analysis and interpretation of the results must be carefully performed. Specifically, we first note that the large-scale motion of the vortices resembles that computed using non-deformable core simulations (Fig. 12), which seems to indicate the same chaotic pattern exhibited by non-deformable core vortices. As a result, chaotic dynamics are also manifested in the more elaborate deformable core model. On their own, these dynamics would place a time-span limitation, beyond which amplification of round-off error alone would cause divergence of a particular solution. More importantly, these difficulties are compounded by the accumulation of spatial discretization errors, which may be amplified by chaotic system dynamics. Thus, the question is whether the discretization is fine enough so that confidence in the computed solution can be established *for the entire simulation.*

To address this issue, comparison of the acoustic source term $U$ in the four cases is performed. The results of this comparison, which is motivated in part by the "sensitivity" of the integral quantity to flowfield dynamics [30], are plotted in Fig. 13. The latter depict the time signals of $U$, for $N_r = 49$, 81, 121, and 169. In the lower resolution runs $N_r = 49$ and 81, acoustic source term predictions are seen to deviate significantly for $t > 2.5$. In the intermediate cases, $N_r = 81$ and 129, the time at which substantial deviation is first detected is slightly delayed. On the other hand, the signals are almost identical for the entire simulation in the higher resolution runs, $N_r = 121$ and 169. Thus, by increasing the spatial resolution, predictions tend to converge. Moreover, the similarity between the computed solutions with $N_r = 121$ and 169 prompts us to stop further refinement; results discussed below are based on the fine discretization having $N_r = 169$.

The observed behavior in the "convergence" of the solution may look surprising, in view of theoretical analyses which indicate an essentially second order in space numerical scheme [24]. Specifically, assuming that spatial errors are amplified exponentially in time at a rate that is "proportional" to the Lyapunov exponent, a relatively modest increase in the number of elements would not be expected to yield an appreciable improvement in the spatial interval over which consecutive refinements agree. In particular, the dramatic improvement obtained as we move from the lower to higher resolution cases may appear strange. However, this behavior may be explained in light of numerical studies which indicate that deterioration in spatial resolution is primarily due to loss of overlap among neighboring elements, as caused by the severe deformation of

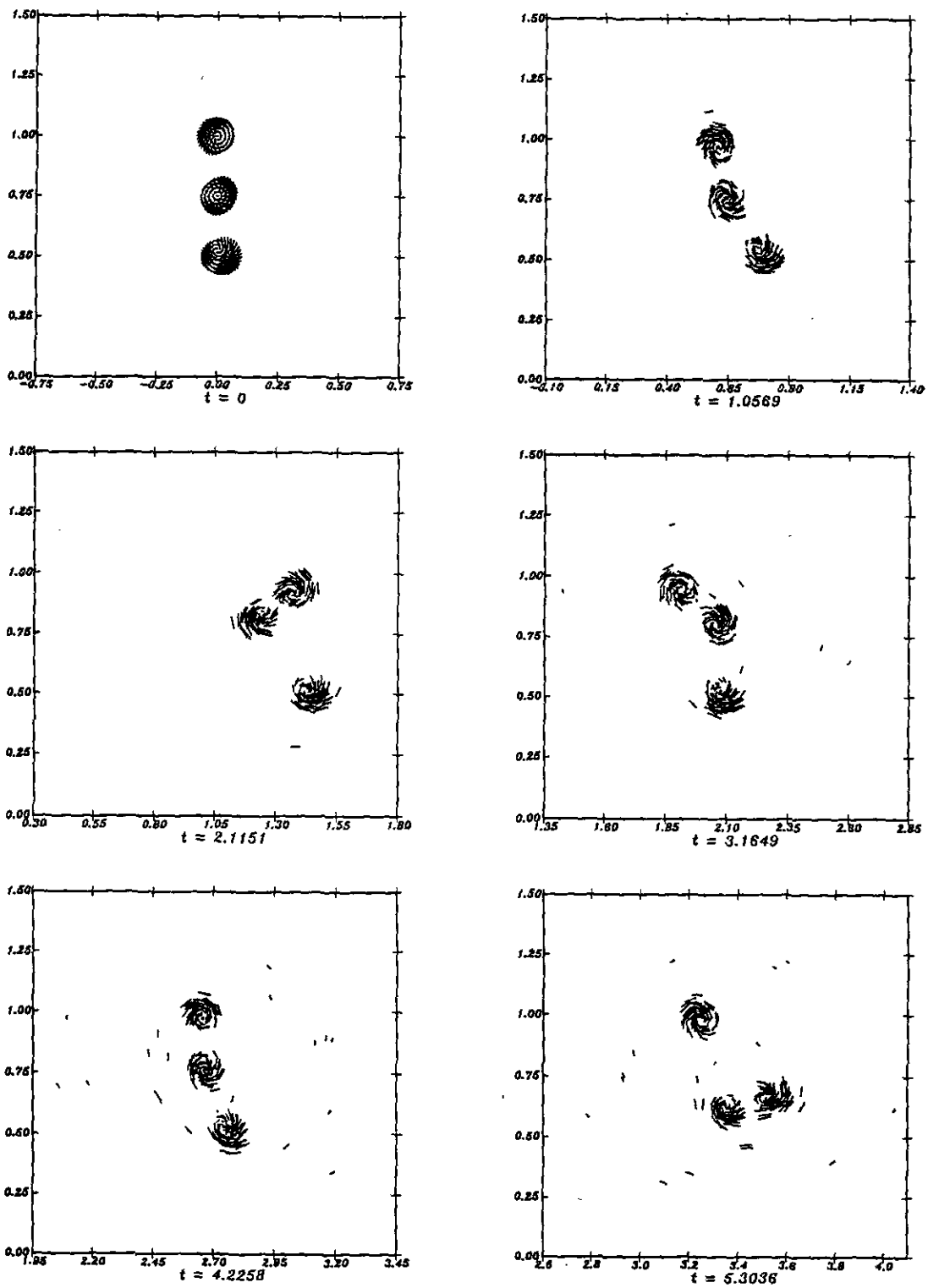


FIG. 9. Vortex element representation of the evolution of the vortex system having $a = 0$ and $\sigma = 0.05$, computed using a grid with $N_r = 81$. The plots are generated by drawing the locations and instantaneous velocity vectors of all vortex elements. Frames are generated every 40,000 computational time steps; elapsed times are indicated.

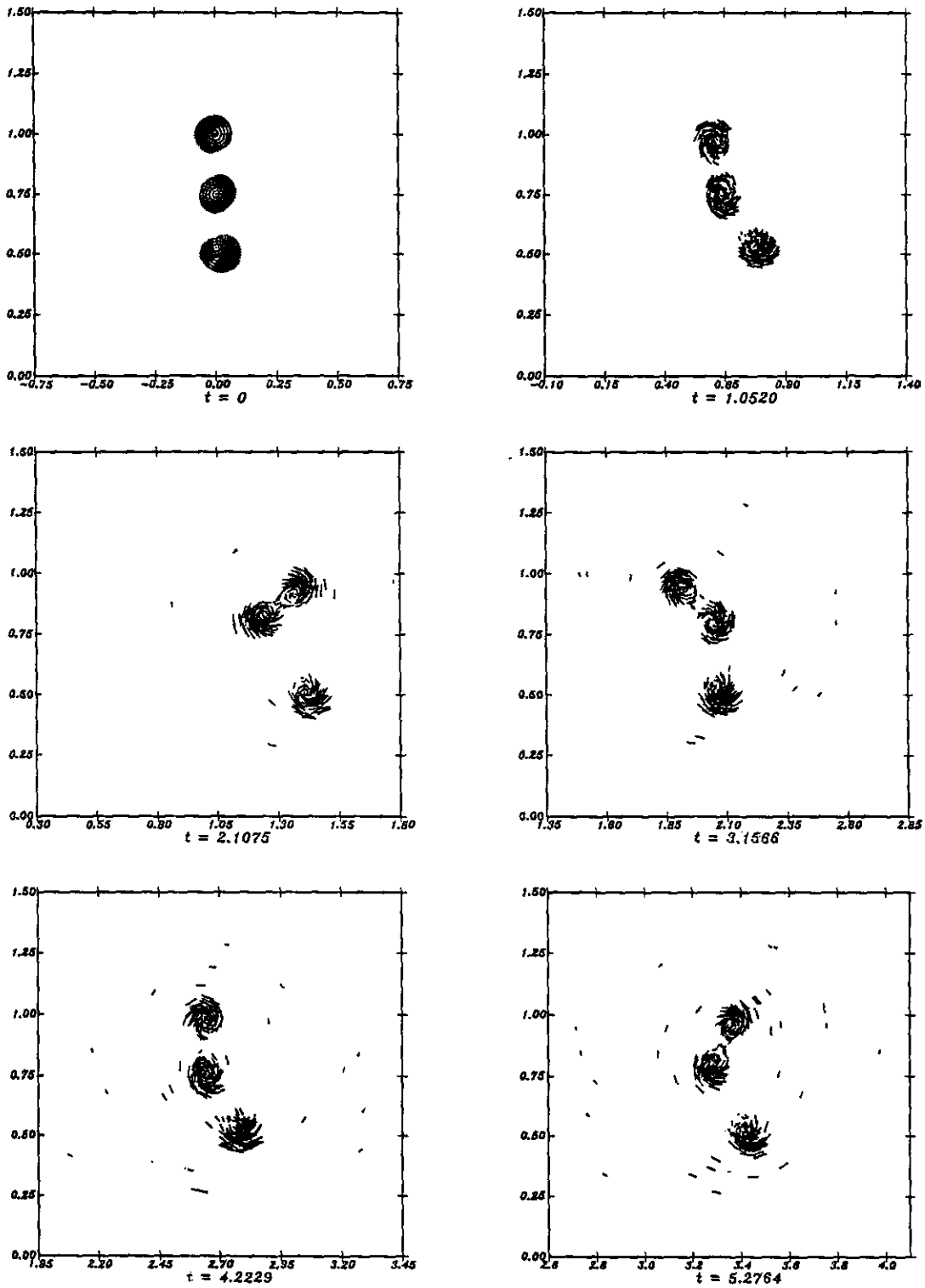


**FIG. 10.** Vortex element representation of the evolution of the vortex system having $a = 0$ and $\sigma = 0.05$, computed using a grid with $N_r = 121$. The plots are generated as in Fig. 9.

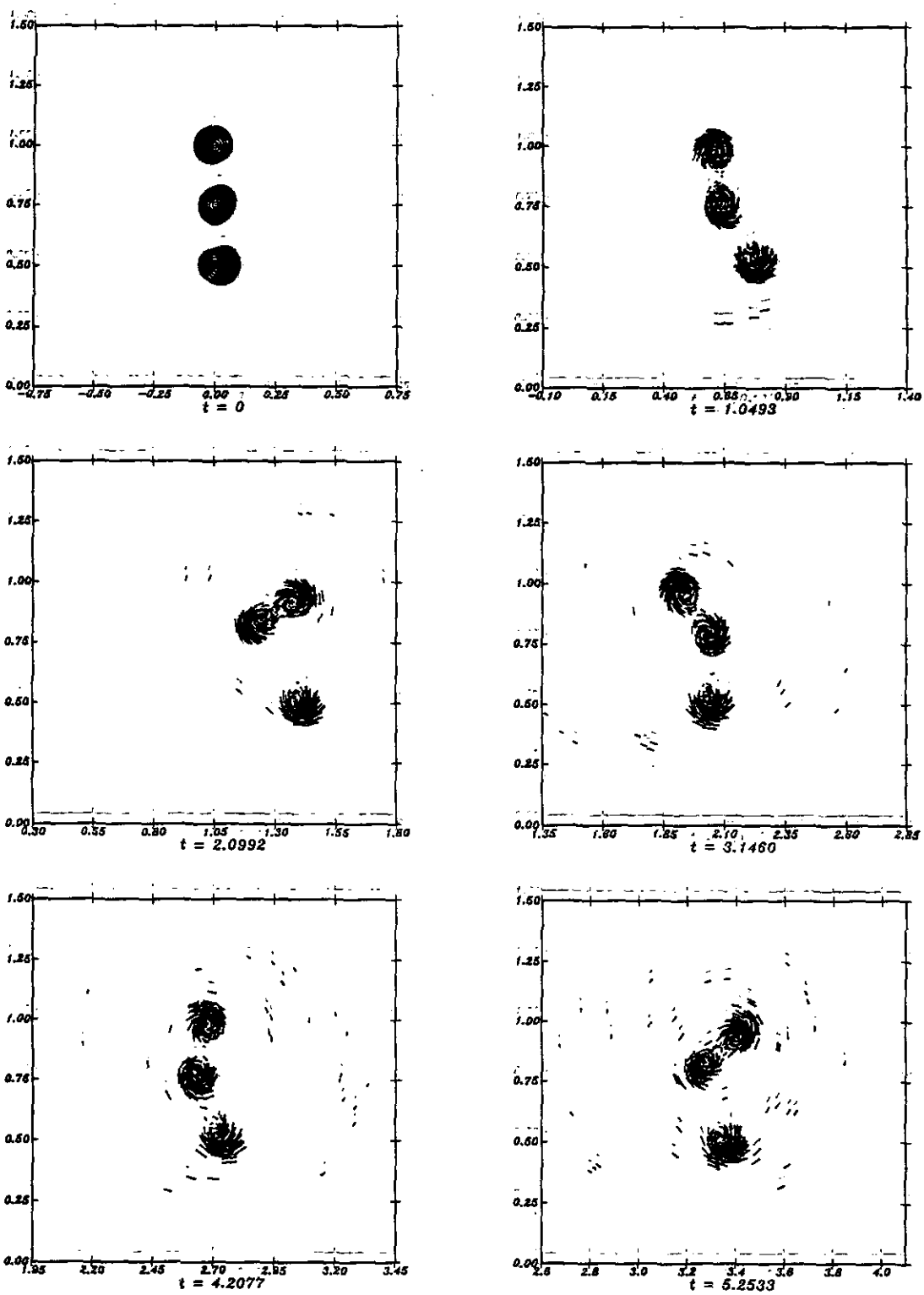


**FIG. 11.** Vortex element representation of the evolution of the vortex system having $a = 0$ and $\sigma = 0.05$, computed using a grid with $N_r = 169$. The plots are generated as in Fig. 9.

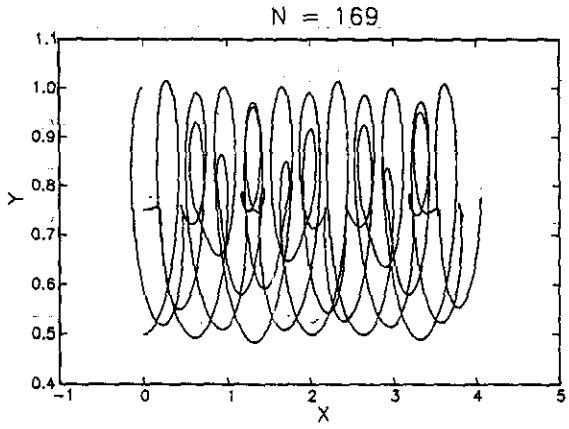


**FIG. 12.** Trajectories of the centroids of the three vortices for the system with $a = 0$ and $\sigma = 0.05$, computed using a grid with $N_r = 169$.

the Lagrangian mesh by the prevailing strain. Since the initial degree of overlap also increases as the resolution is refined, the onset of such a phenomenon is substantially delayed. Thus, the observed behavior is consistent with recent experiences using Lagrangian particle methods [20, 31, 32].

Before discussing radiated noise behavior, we provide two brief comments on (i) the evolution of the system having $a = 0.433$ and (ii) the selection of the core radius in the simulation. Regarding the first item, we note that the large-scale motion of the vortices in this "regular" system also resembles that predicted in the non-deformable model (Figs. 14 and 15). The trajectories of the centroids (Fig. 18) of the vortices are nearly identical to those computed in the non-deformable core model. However, it is interesting to note that in this case the core deformation appears to be much milder than in the chaotic case. This is not surprising since, contrary to the chaotic case, the vortices are always well separated and do not appear to interact (see Figs. 11 and 14).

The selection of the core radius was based on brief numerical experimentation which aimed at avoiding pairing events. This motivation stemmed primarily from our desire to perform a comparison with the results of simpler models, both point-vortex and non-deformable Gaussian simulations. At the same time, selection of very small core radii was undesirable, due to small time-step limitations associated with the very fast spinning motion around the core. Thus, at the start of the study, the two configurations having $a = 0$, $\sigma = 0.1$ and 0.05 were considered. However, for $\sigma = 0.1$, pairing of the three eddies occurred quickly (Fig. 16). Thus, the smaller value of $\sigma$ was chosen for comparison with non-deformable core models and for the numerical study.

*Radiated Noise*

The noise radiated by the system of deformable core vortices is computed using the Powell–Hardin formulation, following the procedure detailed in Section 2.4. We focus first on the system having the initial configuration parameter $a = 0.433$, for which regular trajectories were predicted. The results are given in terms of the acoustic pressure spectrum, plotted in Fig. 17. In computing this spectrum, the same procedure used in previous calculations is adopted; i.e., the time-dependent behavior of the acoustic pressure field is isolated by absorbing constant and spatial terms from the corresponding predictions.

The acoustic pressure spectrum predicted using the deformable core model differs significantly from that derived based on non-deformable core models. For deformable core computations, the pressure spectrum is characterized by two frequency bands. The high-frequency band is characterized by a finite top-hat profile and is distinguished by higher sound levels than those of the low-frequency band. Meanwhile, the low-frequency band resembles that predicted by the non-deformable core model, and the appearance of a discrete set of harmonics can still be detected. Unfortunately, detailed resolution of the corresponding portion of the spectrum could not be performed in this case, since the computations are stopped at a much shorter time than in non-deformable core simulations.

Due to the relative simplicity of the large-scale motion of the system, interpretation of the low-frequency behavior of the acoustic pressure spectrum can be easily provided. To this end, we first recall that the radiated noise is given by time derivatives of second-order moments of vorticity. In turn, these moments may be decomposed into two components: one due to the motion of vorticity centroids—i.e., to large scale vortex motion—and the other associated with the deformation and reorganization of the core vorticity distribution [33]. To emphasize this point, we start with Möhring's [14] "source term,"

$$Q_{ij} = \int x_i(\omega \times \mathbf{x})_j \, d\mathbf{x}, \tag{38}$$

and consider the contribution of a 2D patch of vorticity lying within a circular circumference $S$ and having centroid $\chi$. By defining a coordinate system, $\mathbf{r}$, centered around the centroid of the patch, we may recast Eq. (38) as

$$Q_{ij} = \chi_i(\Gamma \times \chi)_j + \int_S r_i(\omega \times \mathbf{r})_j \, dA, \tag{39}$$

where $\Gamma$ is the (constant) circulation vector of the vorticity patch. Thus, our claim may be justified simply by noting that the first term on the right-hand side of Eq. (39) depends solely on global vortex motion, while the second reflects the internal dynamics of the vortex core.

For the presently considered case ($a = 0.433$), the motion of the vortex centroids are virtually the same as those computed using non-deformable core models. Consequently, by approximating the motion of the system by that of vortex centroids, i.e., by ignoring core deformation, the acoustic pressure spectrum predicted by the simpler models is recovered. In fact, the curves of vortex trajectories and the low-frequency portion of the

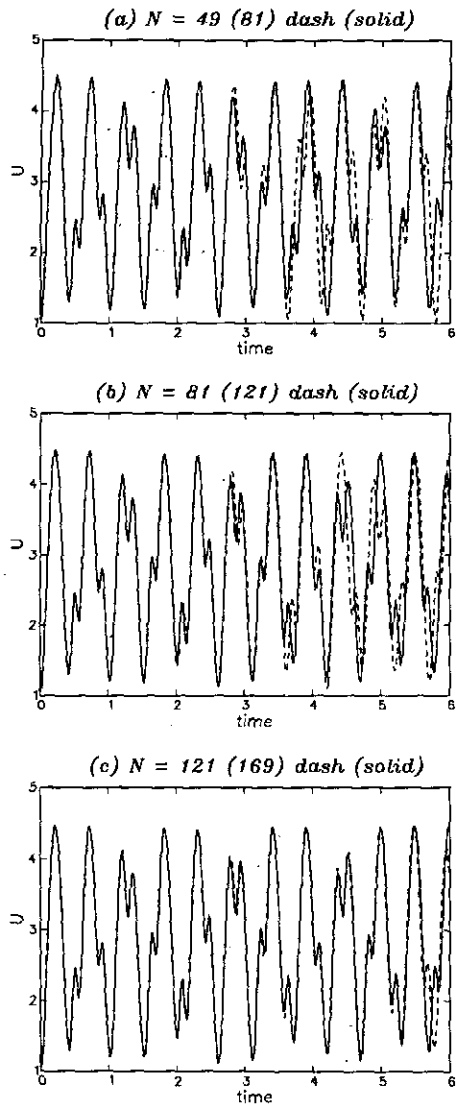


FIG. 13. Comparison of the acoustic source term $U$ for the vortex system having $a = 0$ and $\sigma = 0.05$, computed using grids with (a) $N_r = 49$ and 81; (b) $N_r = 81$ and 121; (c) $N_r = 121$ and 169.

acoustic pressure spectra computed using both deformable and non-deformable core models could not be distinguished in comparison plots. Thus, these plots are omitted.

An immediate consequence of the arguments provided above is that the contribution of the large-scale unsteady vortex motion to radiated noise is restricted to the low-frequency band of the acoustic pressure spectrum. Accordingly, the appearance of the high frequency band is associated with core vorticity reorganization. Although the flowfield illustrations given in Fig. 14 indicate that the vortices remain nearly circular, more detailed analysis reveals that a highly nontrivial motion occurs within their cores. This motion appears to be dominated by inviscid instabilities of the core vorticity distribution, which lead to repeated filamentation of the vortex core (e.g., [34]). The occurrence of a weak inviscid instability was confirmed by independent tests of an isolated perturbed Gaussian vortex (not shown), which also exhibited a core reorganization in the form of a repeated filamentation process.

Acoustic pressure predictions in the chaotic case ($a = 0$) also differ from those based on non-deformable core simulations. These differences are illustrated by comparing the results of Fig. 18, which shows the acoustic spectrum in the deformable core simulation with $N = 169$, with their point-vortex counterpart (Fig. 7). While in both cases a broadband noise scattering is obtained, a much broader frequency spectrum is obtained in deformable core simulations. As in the previous case, the latter are distinguished by the presence of a high-frequency hump centered around the characteristic spinning frequency of individual vortices. However, the peak pressure levels in the high-frequency band are now comparable to the low-frequencies amplitudes. On the other hand, low-frequency noise predictions are similar to those of point-vortex calculations, both concerning the mode of sound emission and acoustic pressure levels. Thus, the high-frequency portion of the pressure spectrum obtained in the more detailed simulation appears as a simple extension of the curve obtained in the frozen core model.

Unfortunately, interpretation of chaotic system simulations requires a more elaborate analysis than that previously performed. In this case, the analysis is faced with additional difficulties due to lack of close agreement between the two models regarding the large-scale system motion. These differences, which could be observed by close inspection of the trajectories of vortex centroids and of point-vortices (e.g., by comparing Figs. 4 and 12), are highlighted in Fig. 19. The figure compares the trajectory of the lower vortex in the frozen core simulations with that of the centroid of the corresponding vortex in the deformable core computations. While these trajectories are in close agreement at early stages, they diverge rapidly at later times. This is not surprising since we do not expect the point-vortex model to hold at all times. In fact, breakdown of the corresponding approximation should be expected in this case, as strong interactions among vortices occur which result in the stripping of fluid layers from the outer edges of their cores.

To overcome this difficulty, comparison between the predictions of deformable and non-deformable core models is performed in two steps. In a first step, we approximate the motion of the system by that of the vortex centroids. Based on this approximation and relying on the Powell–Hardin formulation, we compute an equivalent acoustic source term following the same procedure used in the deformable core model. This source is then differentiated in order to derive a simplified noise spectrum. Next, we rely on the arguments presented earlier in this section and associate this spectrum with the contribution of large-scale motion to noise emission. Thus, the acoustic pressure spectrum is unambiguously decomposed into two components, without resorting to the point-vortex approximation. The results of this analysis are shown in Fig. 20, which depicts pressure spectra obtained using (i) the deformable core model,

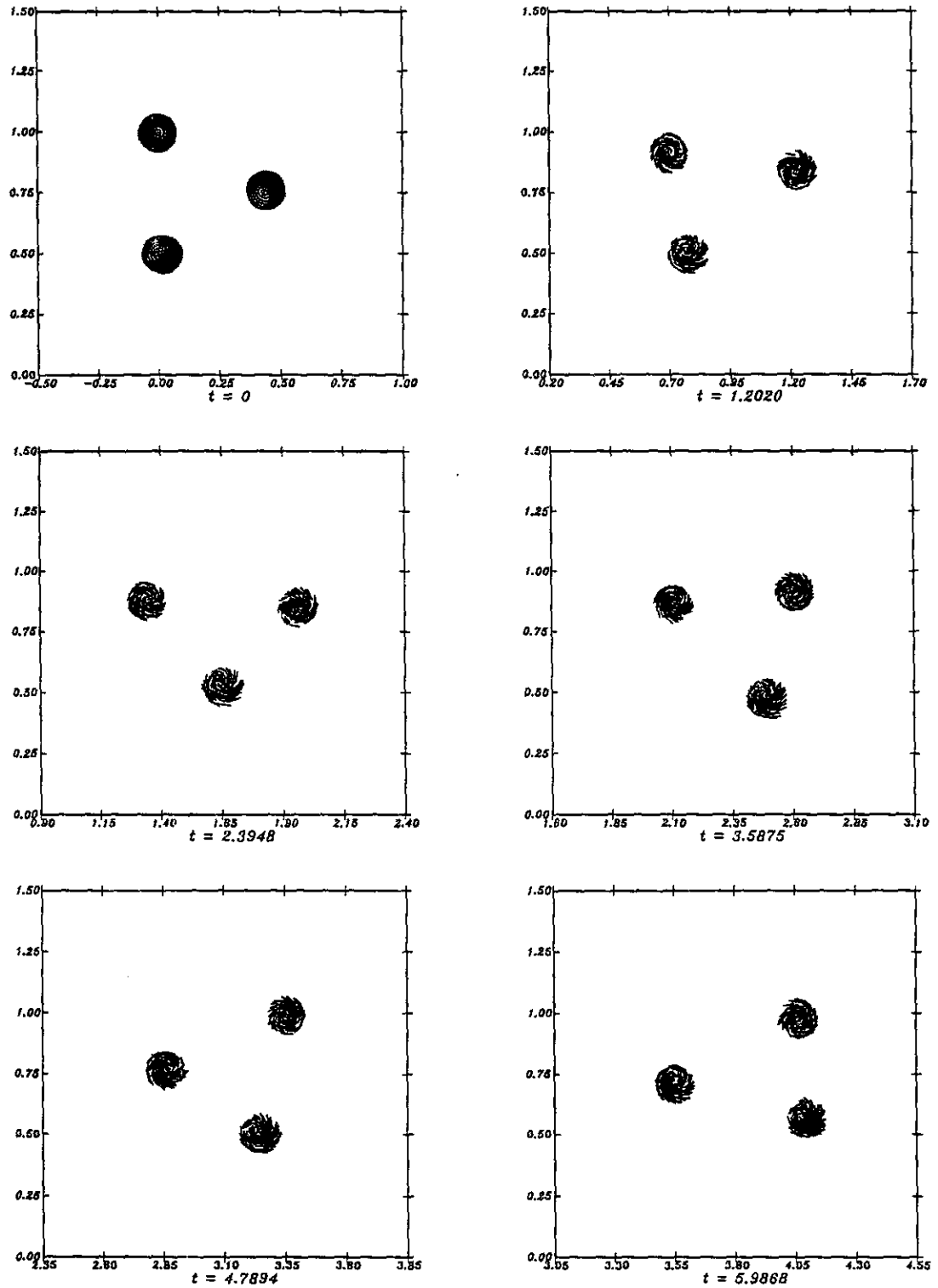


**FIG. 14.** Vortex element representation of the evolution of the vortex system having $a = 0.433$ and $\sigma = 0.05$, computed using a grid with $N_r = 169$. The plots are generated as in Fig. 9.

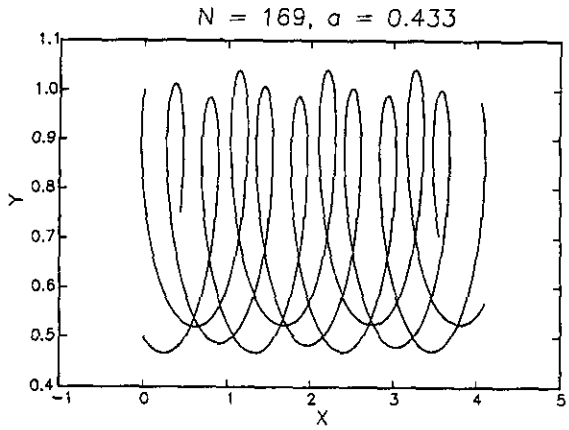


*FIG. 15.* Trajectories of the centroids of the three vortices for the system with $a = 0.433$ and $\sigma = 0.05$, computed using a grid with $N_r = 169$.

(ii) the point-vortex approximation, and (iii) the aforementioned centroid approximation.

The results of this analysis are used to further explore the origin of the high-frequency noise band observed in the deformable core computations. Specifically, the question being posed is whether internal core dynamics lead to the observed high-frequency emission (i) directly, i.e., by direct contribution to the acoustic pressure source term, or (ii) indirectly, by causing high-frequency oscillations in the positions of vortex centroids. The curves shown in Fig. 20 support the former interpretation, since the impact of centroid motion has a small contribution to the high-frequency band observed in deformable core simulations. Consequently, the high-frequency noise band is due to the spinning of the deformed eddy cores. Thus, the corresponding mode of sound emission is associated with "inherently noisy eddies," and not with the large-scale motion of deformable core vortices. On the other hand, low-frequency noise emission appears to be entirely due to large-scale vortex motion. This claim is supported by the fact that all three curves plotted in Fig. 20 yield similar predictions at low frequencies.

## 4. SUMMARY AND CONCLUSIONS

In this work, the noise radiated by the inviscid, unsteady (regular and chaotic) motion of arrays of vortices over a flat slip boundary is numerically investigated using two-dimensional vortex methods. The methods are based on the discretization of the vorticity field into Lagrangian vortex elements. The elements are advected along particle trajectories using the local velocity vector, obtained in terms of a desingularized Biot–Savart convolution.

According to the adopted desingularization approach, different flow models and numerical schemes are obtained. The simplest model considered uses the point-vortex approximation, which collapses the core vorticity into concentrated Dirac masses whose velocities are estimated by removing the singular part from the corresponding Biot–Savart integral. A variant of the point-vortex simulation is also employed with approximates the core vorticity distribution by a frozen Gaussian. In both approaches, vortex core dynamics are ignored and the methods are referred to as non-deformable core models. Core dynamics are directly accounted for in a third approach, which relies on a 2D field method in the simulation of the flow. All three approaches are applied to study flowfield dynamics and to analyze their effect on radiated noise.

Flowfield evolution and dynamics are first interpreted in terms of the initial configuration of the vortex system. The latter consists of an equal-strength 3-vortex system adjacent to a slip plane, arranged in a triangle whose base is fixed and in the direction normal to the boundary. A one-dimensional family of initial configurations is considered by moving the third vortex along the direction of the boundary. Depending on initial conditions, regular or chaotic motion is observed in non-deformable core simulations. Detailed analysis of the vortex trajectories reveals a sharp transition from regular to chaotic motion as the aspect ratio of the initial configuration is decreased.

When regular motion prevails, a discrete far-field sound spectrum is predicted which is dominated by the fundamental spinning frequency of the system and of its superharmonics. Acoustic pressure amplitudes are comparable to the fundamental one for the first few harmonics, but decay rapidly for higher frequencies. Thus, noise emission is limited to a narrow band which is bounded below by the fundamental one.

Dramatic differences in sound radiation are observed when chaotic motion occurs. In this case, broadband noise generation is predicted and the computed sound levels are significantly higher than in the previous case. While in both cases the acoustic spectrum peaks at about the same frequency, the sound amplitude decay at higher frequencies is slower in the chaotic case. Thus, chaotic motion is distinguished by a substantially broader sound radiation.

In all cases considered, the mode of sound emission closely reflects the dynamics of the vortex system. The discrete set of sound frequencies observed when regular motion is predicted coincide with the quasi-periodic spinning of the vortices around the centroid of the system. Similarly, the broadband sound emission predicted for chaotic systems mirrors the complex knotted trajectories of individual point vortices.

It is finally emphasized that, when a "small" core radius is selected, predictions of the frozen-Gaussian model are found to be almost identical to those of the point-vortex approximation. Consequently, results computed using the non-deformable core models are independent of the procedure used to desingularize the Biot–Savart convolution. Thus, as long as core dynamics can be ignored, the models are expected to yield good approximations of the motion of corresponding vorticity distributions. In particular, valid approximations are anticipated whenever concentrated vortices remain well-separated and do not interact vigorously.

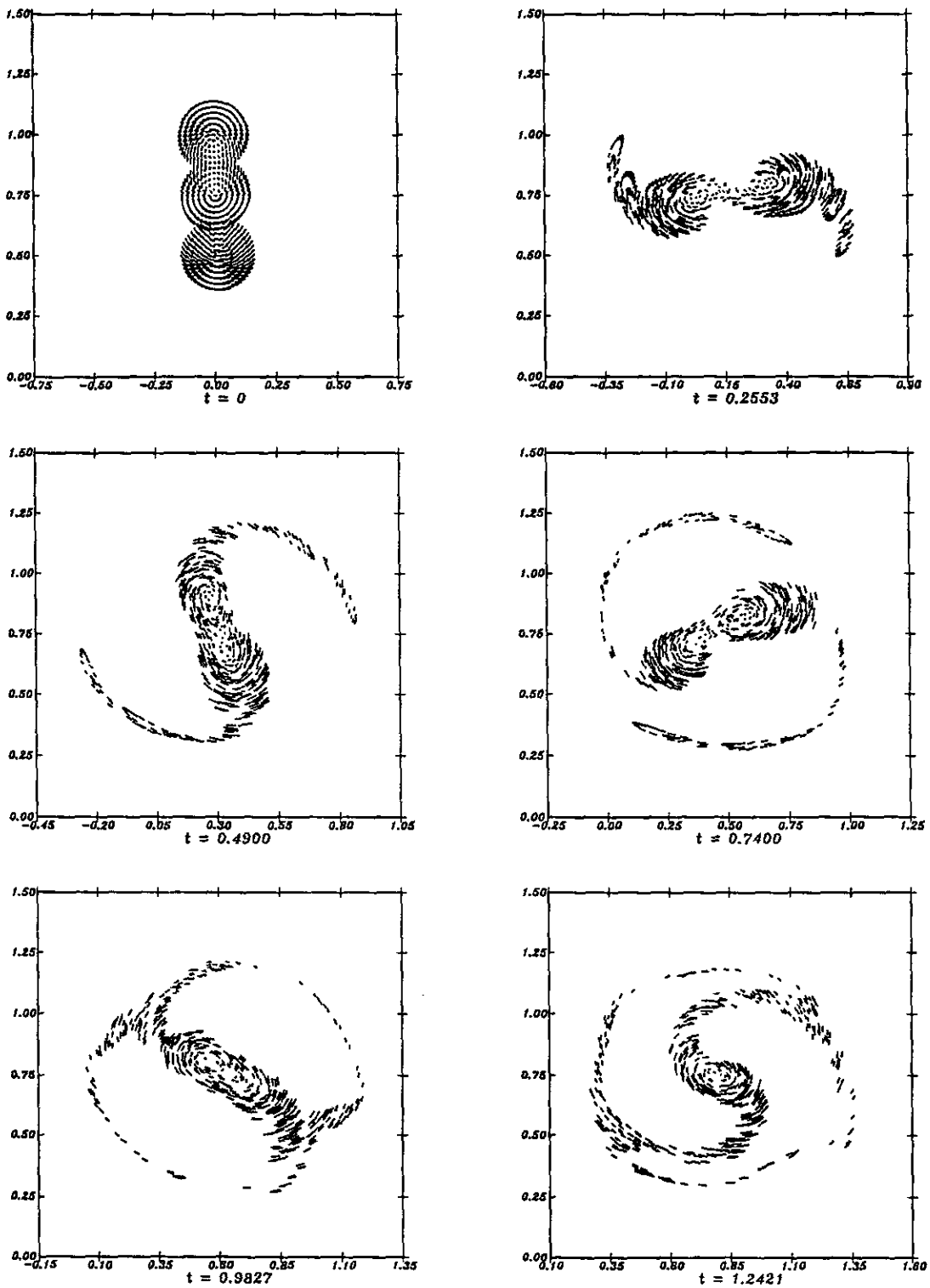


**FIG. 16.** Vortex element representation of the evolution of the vortex system having $a = 0$ and $\sigma = 0.1$, computed using a grid with $N_r = 169$. Frames are generated every 20,000 computational time steps; elapsed times are indicated.

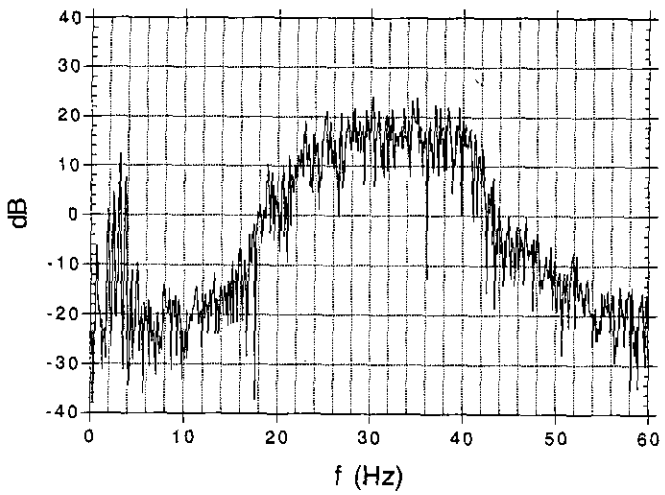


FIG. 17. Acoustic pressure spectrum for a vortex configuration having $a = 0.433$ and $\sigma = 0.05$, computed using a grid with $N_r = 169$. The dependence on listener location has been factored out of the acoustic pressure prediction before computing the spectrum.

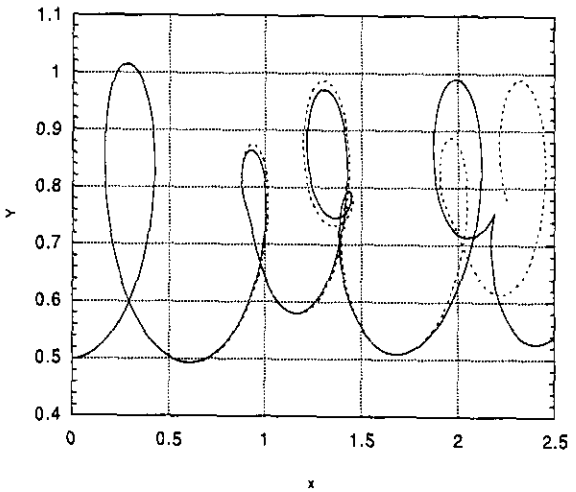


FIG. 19. Comparison of vortex trajectories for an initial configuration with $a = 0$, $\sigma = 0.05$, computed using point–vortex calculations (solid) and a deformable core model with $N_r = 169$ (dash).

The impact of internal core dynamics on the behavior of the system and radiated noise are finally examined using a two-dimensional vortex element method. Implementation of the method is based on discretization of the vortex cores using a large number of smooth vortex elements. Numerical study of computed solutions is first performed in order to determine the effects of the discretization. When chaotic motion occurs, it is shown that a fine core discretization is necessary to ensure that the large-scale features of the solution are independent of the choice of numerical parameters. Thus, an appropriate refinement is first determined, based on the motion having the highest Lyapunov exponent, and subsequently used in all deformable core computations.

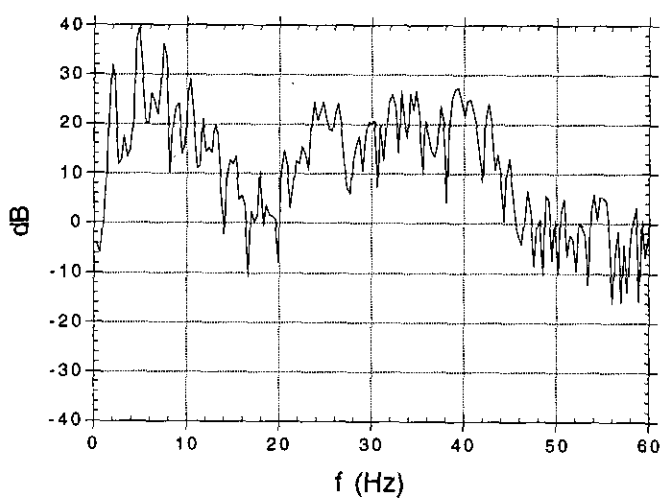


FIG. 18. Acoustic pressure spectrum for a vortex configuration having $a = 0$ and $\sigma = 0.05$, computed using a grid with $N_r = 169$. The dependence on listener location has been factored out of the acoustic pressure prediction before computing the spectrum.

When regular motion occurs, core dynamics have little impact on the large-scale features of the system. In this case, the trajectories of the centroids of the vortices are found to be almost identical to those predicted by non-deformable core models. All models yield similar low-frequency noise emission. However, in deformable core simulations, the sound spectrum is distinguished by the appearance of a high-frequency band which is centered around the spinning frequency of the individual vortices. The sound spectrum is dominated by the high frequency emission, as the corresponding pressure amplitudes are significantly higher than low-frequency peak levels. Thus, the internal motion within vortex cores substantially alters the far-field sound signature.

On the other hand, internal core dynamics are found to affect chaotic vortex motion. Departures from non-deformable core approximations are recorded following strong interactions, during which vortex cores approach each other and stripping of fluid layers from their outer edges occurs. During such events, vortices are subjected to violent strain fields, which result in a large deformation of their cores and the loss of the initial circular shape. However, the trajectories of the centroids retain a shape which is similar to their point-vortex counterparts, and the complex knotted pattern observed in non-deformable core simulations persists.

Despite differences in computed vortex trajectories, all models yield similar low-frequency sound prediction. However, as in the regular case, the generation of a high-frequency noise band is recorded in deformable core computations. But unlike the previous case, the high-frequency noise band does not dominate the sound spectrum, as the corresponding pressure levels are of the same order as the low-frequency peaks.

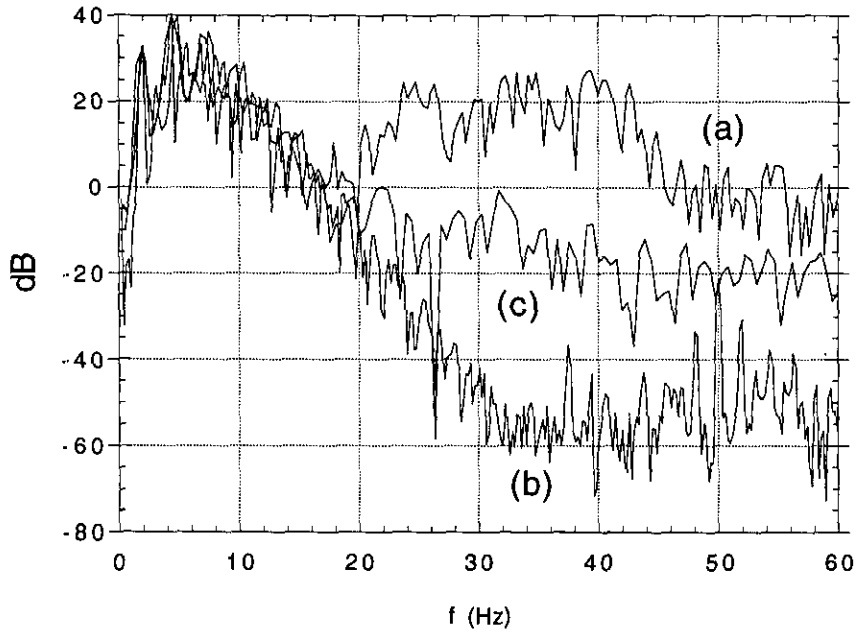


**FIG. 20.** Acoustic pressure spectra for the system having $a = 0$, $\sigma = 0.05$, predicted by (a) the deformable core model with $N_r = 169$; (b) the point-vortex approximation; and (c) approximating the motion of deformable vortices by that of their centroids. The dependence on listener location has been factored out of the acoustic pressure prediction before computing the spectrum.

Analysis of the origin of this phenomenon points to a weak inviscid instability within the Gaussian cores, whose growth of the instability is amplified by the prevailing strain field induced by all the vortices. Maturation of this instability leads to a reorganization of the core vorticity distribution in the form of a repeated filamentation process. It is shown that the high-frequency noise radiation is directly due to the spinning of deformed vortices.

Finally, we should emphasize that the present study of the impact of core dynamics is restricted to a relatively narrow set of initial conditions. By choosing a small value of the core radius, which enables comparison with non-deformable core models, detailed experimentation with different core radii is avoided. Furthermore, analysis of the differences between model predictions is limited to an investigation of the origin of these differences and of their relationship to system dynamics. Thus, in-depth investigation of the fine details of internal core motion and of their impact on noise emission is omitted. This omission is on one hand due to the necessity of even finer refinements than those considered here. On the other, the authors believe that the exercise should be conducted using a simpler configuration, in order to avoid simultaneously tackling chaotic system dynamics and the complexity spawned by small-scale internal core motion.

## ACKNOWLEDGMENTS

The work of the first author was performed while he was a visiting scholar at the Centre Acoustique of the Ecole Centrale de Lyon. A preliminary version of the results was presented at the "*13 ème Colloque d'Aéro- et Hydro-Acoustique*" held at the Ecole Centrale de Lyon in June 1993. The authors acknowledge useful discussions with Professors G. Comte-Bellot, J. E. Ffowcs-Williams, and P. Moin.

## REFERENCES

1. H. Aref, *Ann. Rev. Fluid Mech.* **15,** 345 (1983).
2. E. A. Novikov, *Sov. Phys. JETP* **41,** 937 (1975).
3. H. Aref, *Phys. Fluids* **22,** 393 (1979).
4. E. A. Novikov and Y. B. Sedov, *Sov. Phys. JETP* **48,** 440 (1978).
5. H. Aref and N. Pomphrey, *Proc. R. Soc. London A* **380,** 359 (1982).
6. G. S. Murty and K. S. Rao, *J. Fluid Mech.* **40,** 595 (1966).
7. H. Aref, in *Proceedings, 16th International Congress of Theoretical and Applied Mechanics North-Holland, Amsterdam, 1984), p. 43.*
8. A. T. Conlisk, Y. G. Guezennec, and G. S. Elliot, *Phys. Fluids A* **1,** 704 (1989).
9. L. Collorec, D. Juvé, and G. Comte-Bellot, in *Computational Aeroacoustics,* edited by J. C. Hardin and M. Y. Hussaini, p. 174.
10. Y. Kimura, I. Zawadki, and H. Aref, 1990. *Phys. Fluids A* **2,** 214 (1990).
11. M. J. Lighthill, *Proc. R. Soc. London A* **211,** 564 (1952).
12. A. Powell, *J. Acoust. Soc. Am.* **36,** 177 (1964).
13. J. C. Hardin, 1977. "Noise Calculation on the Basis of Vortex Flow Models," *ASME Symposium on Noise and Fluid Engineering, Atlanta, GA, 1977.*
14. W. Möhring, *J. Fluid Mech.* **85,** 685 (1977).
15. J. E. Ffowcs-Williams, 1982. *AIAA J.* **20,** 307 (1982).
16. H. Lamb, *Hydrodynamics* (Dover, New York, 1932).
17. B. E. Mitchell, S. K. Lele, and P. Moin, AIAA Paper 92-0374, 1992 (unpublished).

18. G. K. Batchelor, *An Introduction to Fluid Dynamics* (Cambridge Univ. Press, Cambridge, 1967), p. 86.
19. O. M. Knio and A. F. Ghoniem, in *Vortex Flows and Related Numerical Methods* (Kluwer, Dordrecht, 1993), p. 341.
20. A. F. Ghoniem, G. Heidarinejad, and A. Krishnan, *J. Comput. Phys.* **79,** 135 (1988).
21. J. T. Beale and A. Majda, *Math. Comput.* **39,** 1 (1982).
22. J. T. Beale, and A. Majda, *Math. Comput.* **39,** 29 (1982).
23. J. T. Beale, 1986. *Math. Comput.* **46,** 401 (1986).
24. J. T. Beale and A. Majda, *J. Comput. Phys.* **58,** 188 (1985).
25. O. M. Knio and A. F. Ghoniem, *J. Comput. Phys.* **86,** 75 (1990).
26. T. Kambe, *J. Fluid Mech.* **173,** 643 (1986).
27. R. P. Weston and C. H. Lu, AIAA Paper 82-0951 (unpublished).
28. A. Wolf, J. B. Swift, H. L. Swinney, and J. A. Vastano, *Physica D* **16,** 285 (1985).
29. W. Magnus, F. Oberhettinger, and R. P. Soni, *Formulas and Theorems for the Special Functions of Mathematical Physics* (Springer-Verlag, New York/Berlin, 1966), p. 80.
30. J. Bridges and F. Hussain, *J. Fluid Mech.* **240,** 469 (1992).
31. S. Huberson, A. Jollès, and W. Shen, 1991. *Lectures in Applied Math.*, Vol. 28 (Am. Math. Soc., Providence, RI, 1991), p. 369.
32. O. M. Knio and A. F. Ghoniem, *J. Comput. Phys.* **97,** 172 (1991).
33. M. H. Krane and L. Collorec, *Acta Acustica,* to appear.
34. D. G. Dritschel, 1987. "The Repeated Filamentation of Vorticity Interfaces," *IUTAM Symposium on Fundamental Aspects of Vortex Motion, Tokyo, Japan, 1987.*